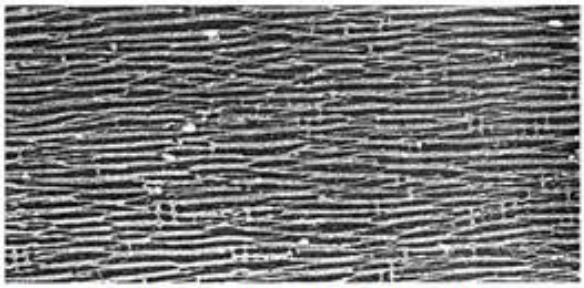

Fig. 1 The Alnico microstructure

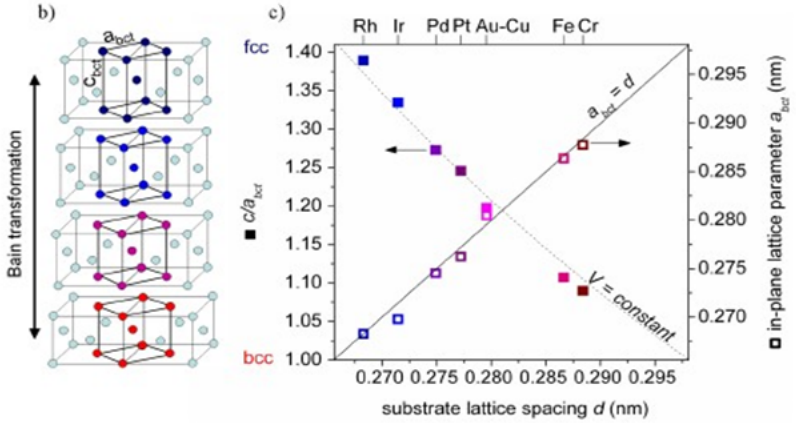

Fig. 2. Transformation connecting fcc (top, blue) and bcc (bottom, red) structure by a continuous variation of the tetragonal distortion (c/a_{bct} ratio). Right: Stabilisation of intermediate stages during this transformation path by coherent epitaxial growth. For the $F_{70}Pd_{30}$ system buffer materials (as marked on the top) exhibiting different substrate lattice spacings are used. This determines the in-plane lattice parameters of the F70Pd30 film (right axis) and since the volume V remains almost constant, the tetragonal distortion can be varied almost from bcc ($c/a_{bct}=1$) to fcc ($c/a_{bct}=\sqrt{2}$)

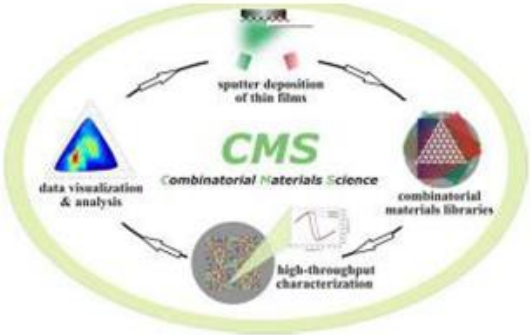

Fig. 3 Schematic of Combinatorial Materials Science

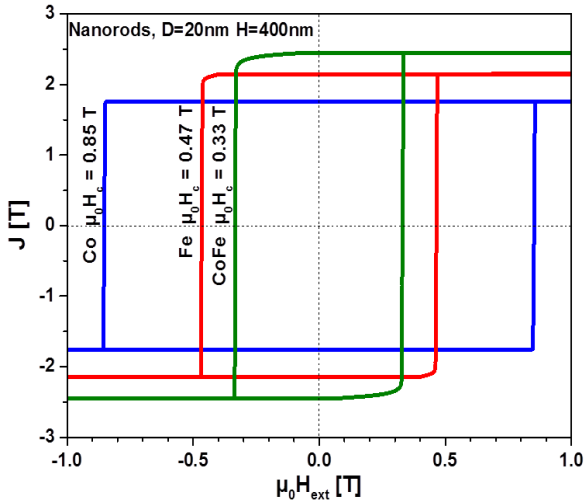

Fig. 4. Hysteresis of a single Co, Fe and CoFe *nanorod with the same dimensions.*

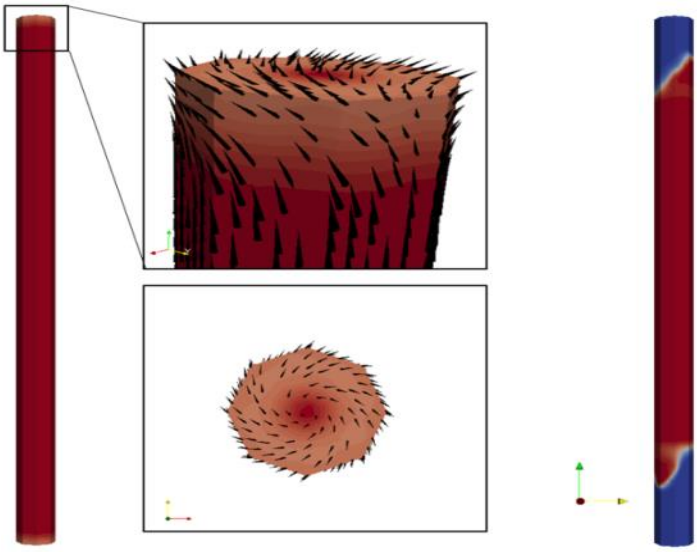

Fig 5.. Nucleation and incoherent magnetization reversal in a high-aspect-ratio Co nanorod. The demagnetizing field at the tips causes a curling-like vortex structure. The magnetization reversal is an incoherent process involving the movement of two domain walls from the tips to the center of the nanorod

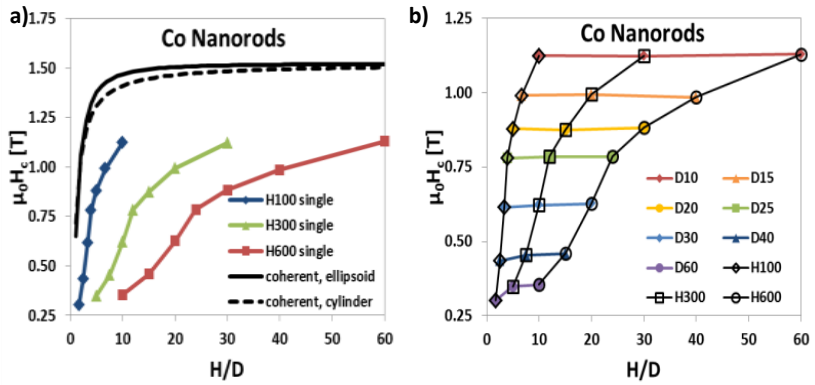

Fig. 6. a) Theoretical upper limit of coercivity of Co nanorods as function of the aspect ratio H/D with simulation results. b) Simulated coercivity as function of aspect ratio with lines of constant height and diameter.

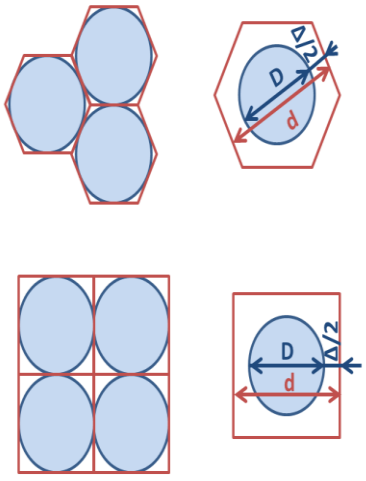

Packing Nanorods with D=10nm			
d [nm]	Δ [nm]	p_{hex}	p_{quad}
10	0	0.907	0.785
11	1	0.750	0.649
12	2	0.630	0.545
13	3	0.537	0.465
14	4	0.463	0.401
15	5	0.403	0.349
20	10	0.227	0.196
30	20	0.101	0.087
40	30	0.057	0.049

Fig. 7. Hexagonal and quadratic packing of nanorods with diameter D, center-center distance d and surface-surface-distance (wall thickness) Δ.

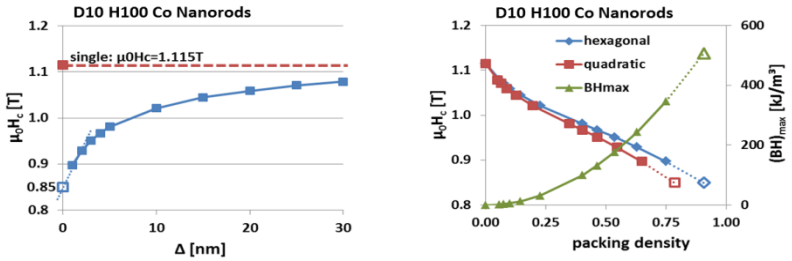

Fig. 8. a) Coercivity of two parallel interacting nanorods with distance Δ. The coercivity of a single nanorod acts as upper coercivity limit with indefinitely high distance. b) Coercivity values in (a) transformed as function of packing density and the resulting energy density product.

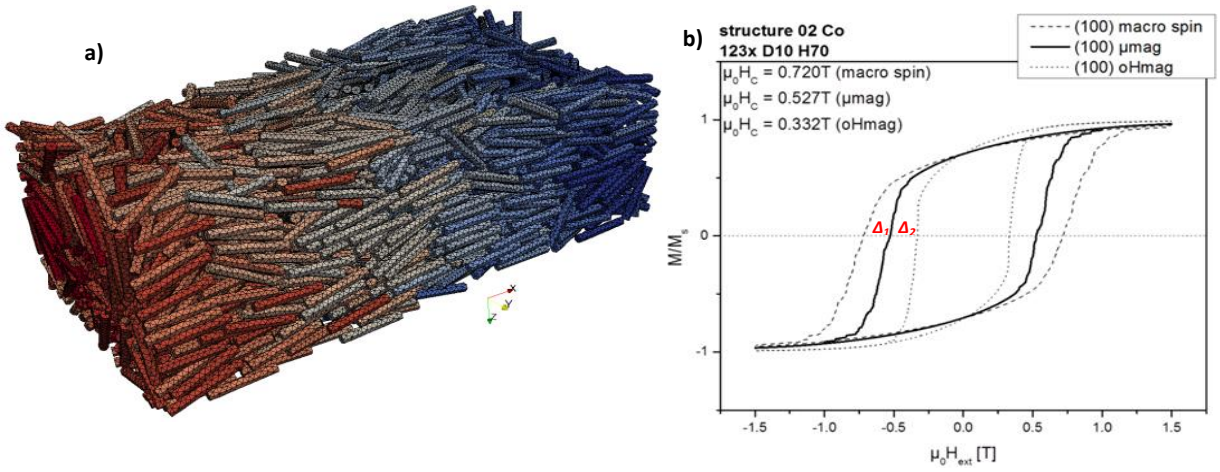

Fig 9. a) Finite element model of a Co structure with 3200 nanorods. b) Calculated hysteresis properties according to the three simulation methods: Full micromagnetics (μmag) give the most accurate results, macro spin assumes coherent reversal and H_{mag} takes only crystal anisotropy into account. These simulation modes make it possible to calculate the loss due to incoherent reversal modes (Δ_1) and the gain due to shape anisotropy (Δ_2)

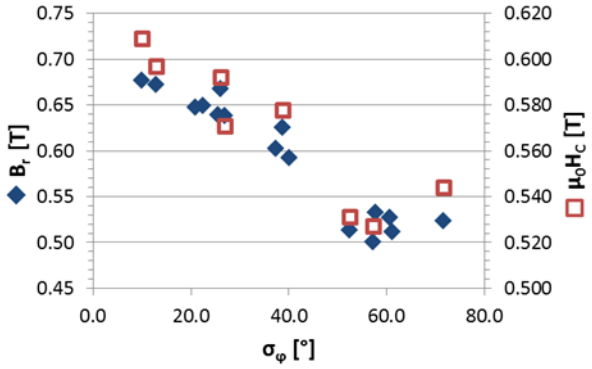

Fig 10. Dependence of remanence (diamonds) and coercivity fields (squares) on misalignment σ_ϕ. The data shows a linear decrease of both remanence and coercivity with increasing misalignment.

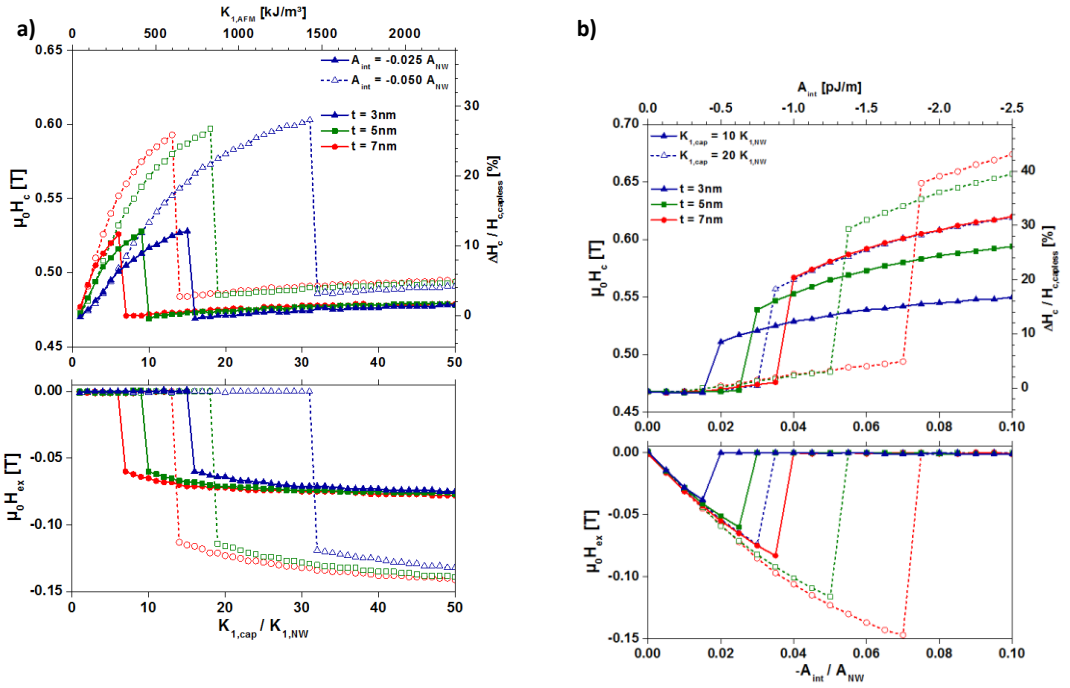

Fig. 11. Coercive and bias field as function of a) magnetocrystalline anisotropy of the capping layer b) exchange between nanorod and capping layer.

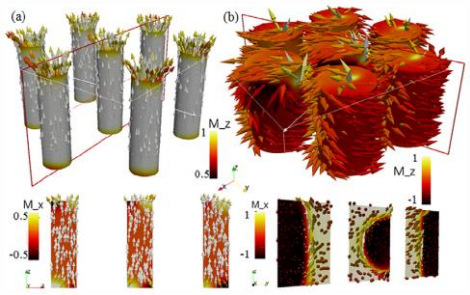

Fig12.- Simulated remanence magnetization for arrays of 7 nanopillars with diameter D= 35nm (a) and 75 nm (b). Arrows indicate the magnetization direction and colors the longitudinal Mz (up) and transverse Mx magnetization on 3D images (up).

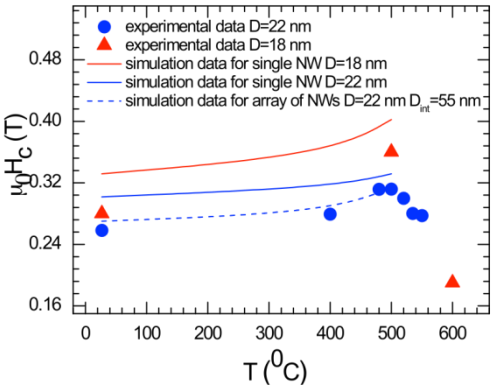

Fig 13. Experimental (filled symbols) RT evolution of coercivity with the annealing temperature for CoFeCu nanowires of indicated diameter, D_w, and corresponding simulations for a single nanowire (lines) and for an array of 7 nanowires (dashed line).

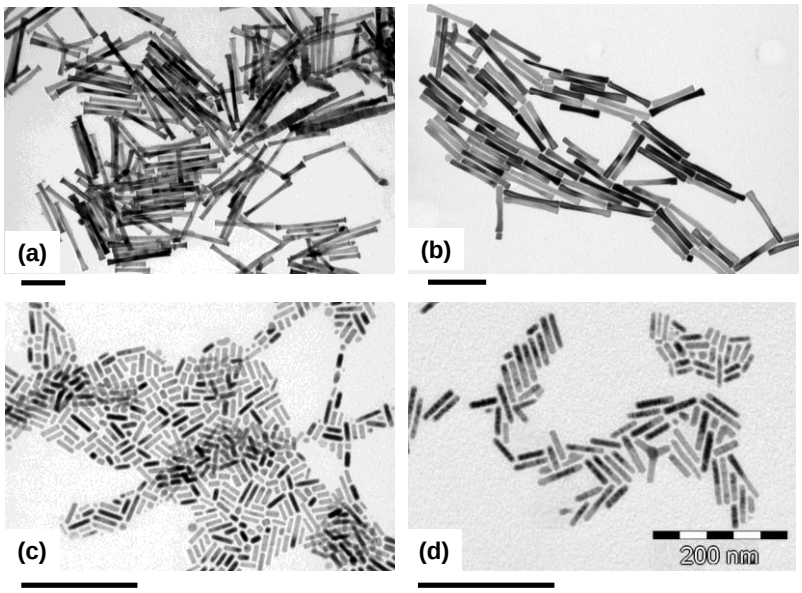

Fig 14. TEM images of cobalt nanorods synthesized by the polyol process (a) and (b) with classical heating mantle, (c) and (d) with a microwave oven (Scale bar denotes 200 nm). Mean diameter, D_m, and mean length, L_m: (a) D_m = 18 nm, L_m = 280 nm; (b) D_m = 16 nm, L_m = 160 nm; (c) D_m = 7.5 nm, L_m = 28 nm; D_m = 8 nm, L_m = 42 nm. Sample (a) was prepared with 2.5% of hydrated $RuCl_3$ ref. Sigma Aldrich 463779; (b) with 2.5 % of hydrated $RuCl_3$ ref. Sigma Aldrich 84050; (c) and (d) with 2.5% and 2 % of anhydrous $RuCl_3$ ref. Sigma Aldrich 208523 as nucleating agent.

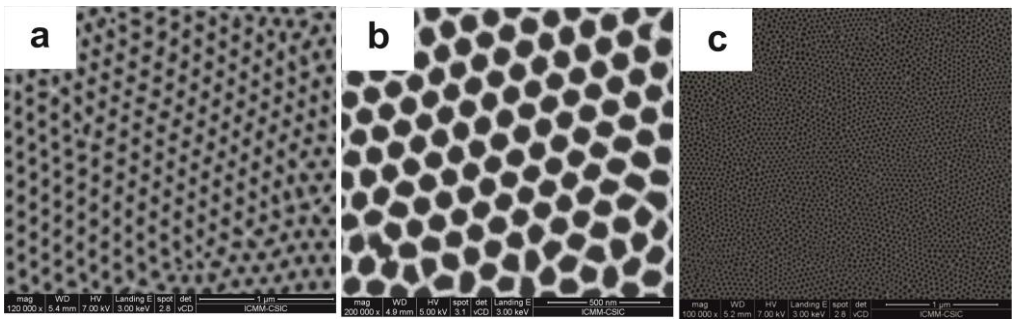

Fig15. Top view SEM images of AAO membranes with pores of: (a) 40nm in diameter and 105 interpore distance, (b) 80nm in diameter and 105nm interpore distance and (c)18nm and 50nm interpore distance.

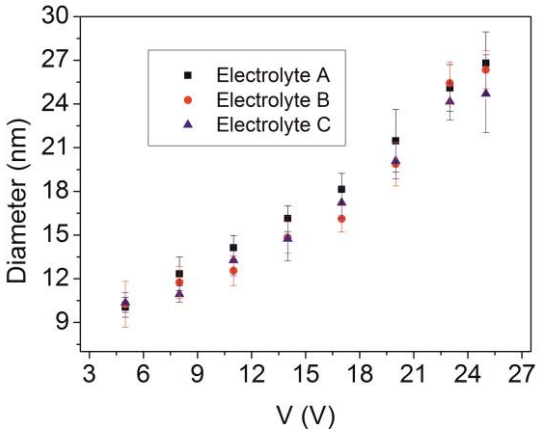

Fig 16. Dependence of pore diameter for different electrolyte concentrations (A, B and C series) on applied voltages.

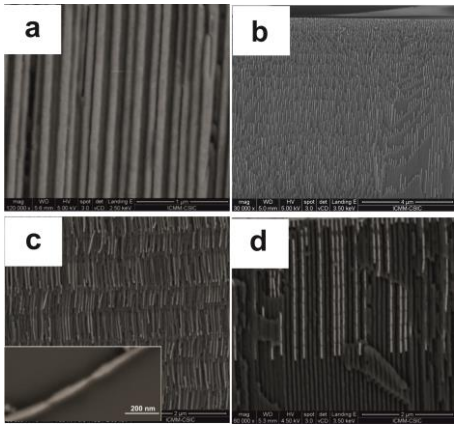

Fig.17. Cross-section SEM images of a) CoFe nanowires with diameters of 80nm, b) CoFeCu nanowires with diameters of 20nm, c) CoFeCu nanowires with modulated diameters and d) CoFe/Au multilayered nanowires with 40 nm in diameter. The insert shows a close-up image of modulated nanowires in (c).

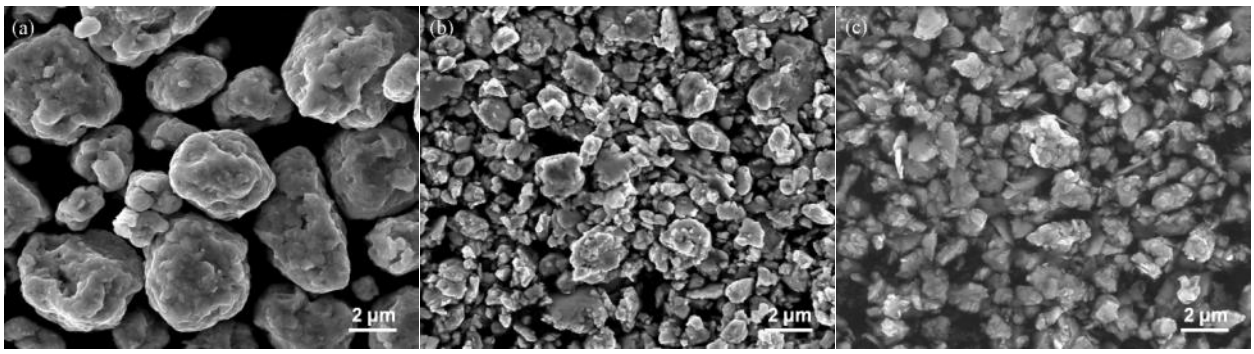

Fig.18. SEM images of ball milled Fe1.5Co0.5B samples for (a) dry milling, (b) wet milling under ethanol and (c) wet milling under heptane and oleic acid (surfactant assisted). For comparison of the particle size the same rotational speed and milling time was used for all samples.

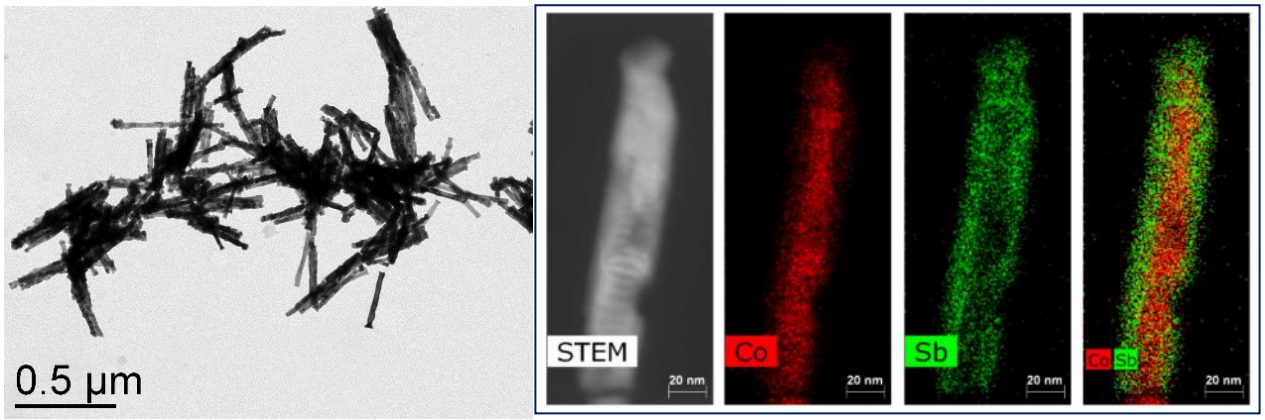

Fig. 19. (a) Bright field TEM image of a core-shell Co/CoSb nanorod obtained by the decomposition of antimony acetate in oleylamine at 250°C (Co:Sb ratio = 4:1); (b) STEM-HAADF image (left) and corresponding EDX analysis (right) of a single rod (Co map in red, Sb map in green and combined map of Co and Sb).

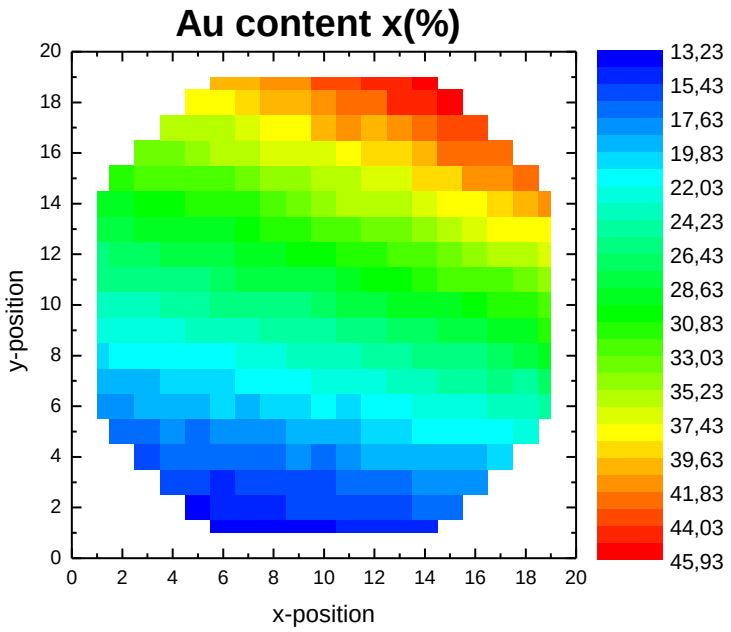

Fig 20. Compositional spread of Au content x(%) in Au_xCu_{1-x} buffer layer library

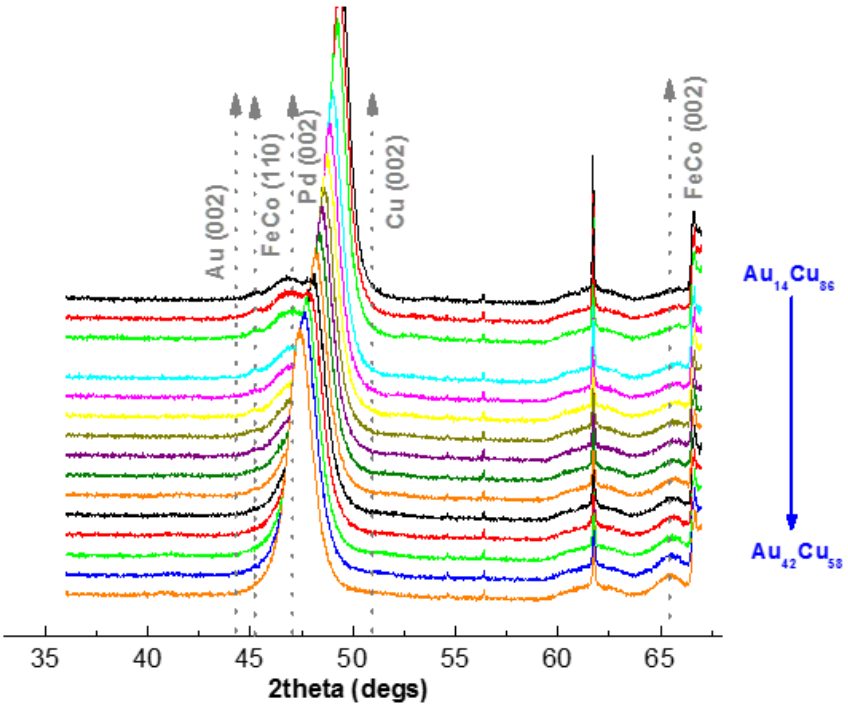

Figure 21. X-ray spectra for a 30 nm thick FeCo thin film deposited on a Au_xCu_{1-x}/Pd/Cu/Si substrate.

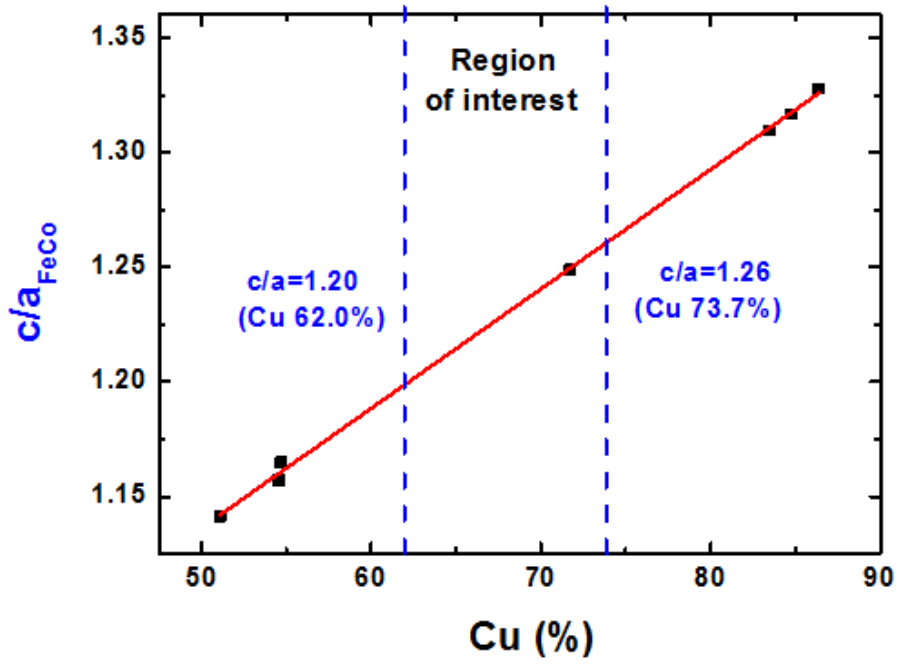

Figure 22. c/a ratio of FeCo as a function of the Cu content in the AuxCu1-x buffer layer.

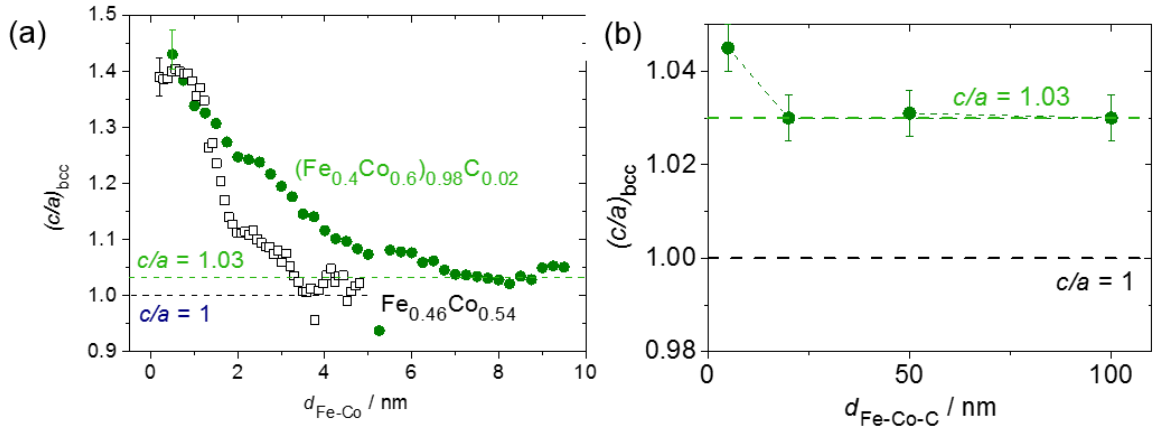

Fig 23: a) Comparison of ternary $(Fe_{0.4}Co_{0.6})_{0.98}C_{0.02}$ with binary Fe-Co strain relaxation during growth detected with in situ RHEED. b) c/a ratios of tetragonal distortion from texture XRD measurements of $(Fe_{0.4}Co_{0.6})_{0.98}C_{0.02}$ films in dependence on film thickness.

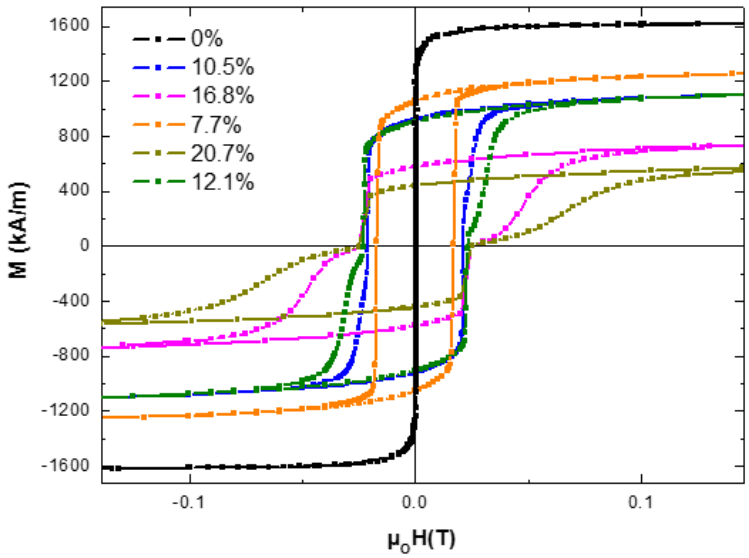

Figure 24: Hysteresis loops of Fe-Co-Nb for average Nb contents from 0 to 21 at. %

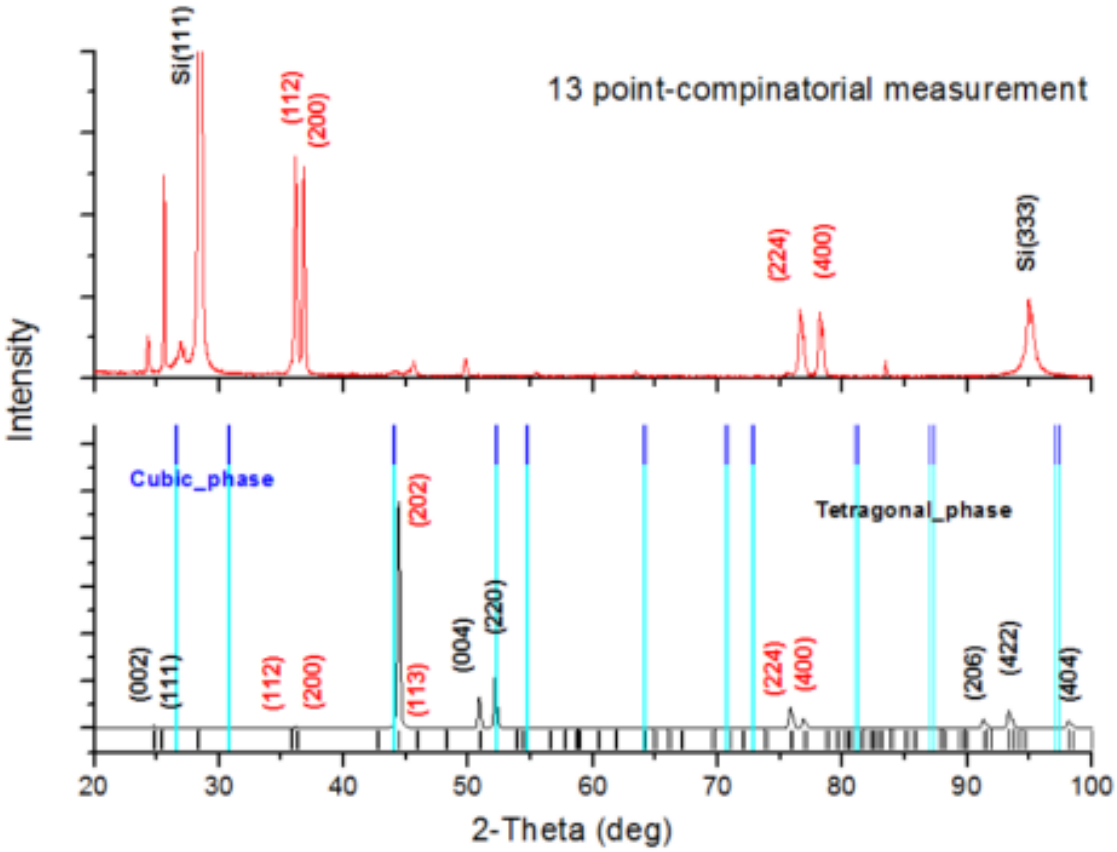

Fig 25: Calculated X-ray diffraction pattern for the tetragonal Heusler alloy (up) and the X-ray diffraction pattern of Fe_2CuGa on Si (111) (below) sample are shown. The peaks of the regular cubic structure are presented in blue color.

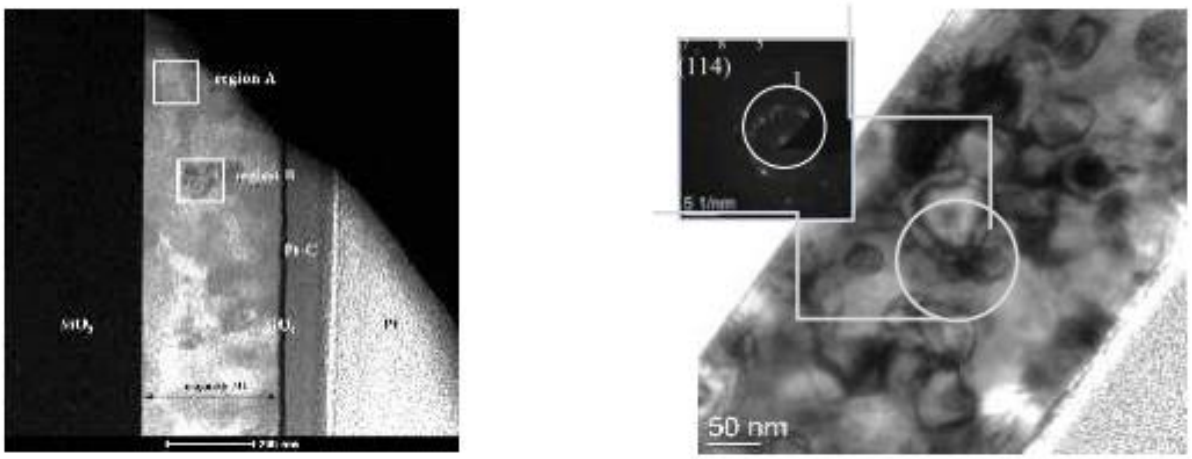

Fig 26: Z-contrast image of the cross section (left) and bright field image with indexed pattern showing a granular microstructure (right) of Fe/Co/Nb multilayers

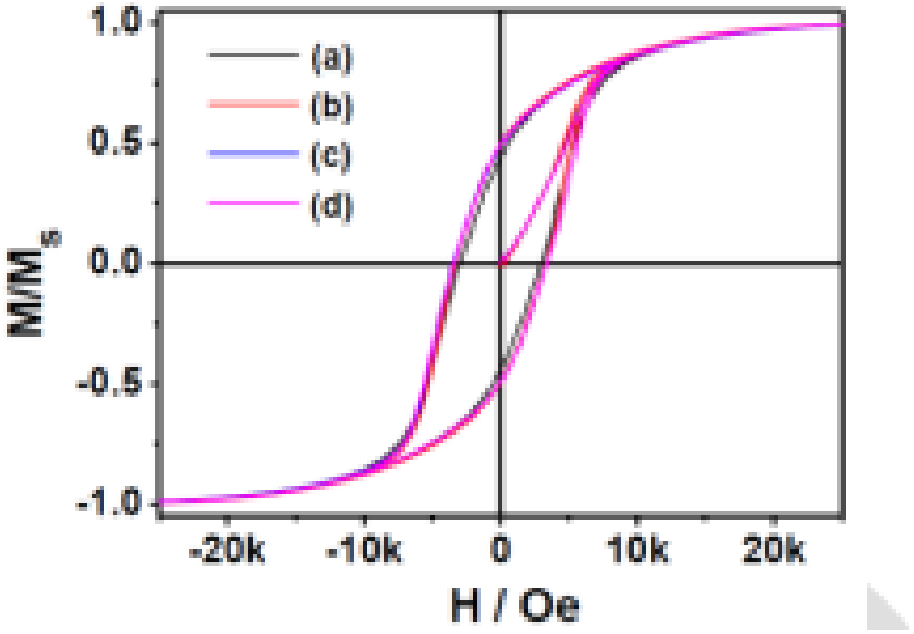

Figure 27: Magnetization loop at room temperature of the raw Co nanorods (a); Co@CoSb with Co/Sb=8 (b); Co@CoSb with Co/Sb= 4 (c); Co@CoSb with Co/Sb= 2 (d).

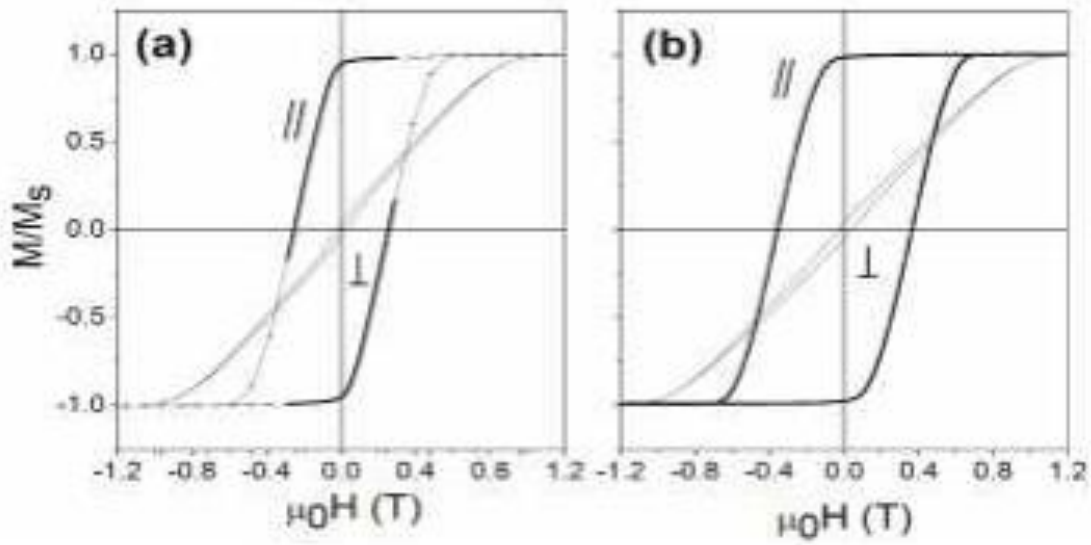

Fig 28: Parallel and perpendicular hysteresis loops for the 18nm diameter nanowire array in as-deposited (a) and 500 ºC annealed (b). The EMD lies along the nanowire axis

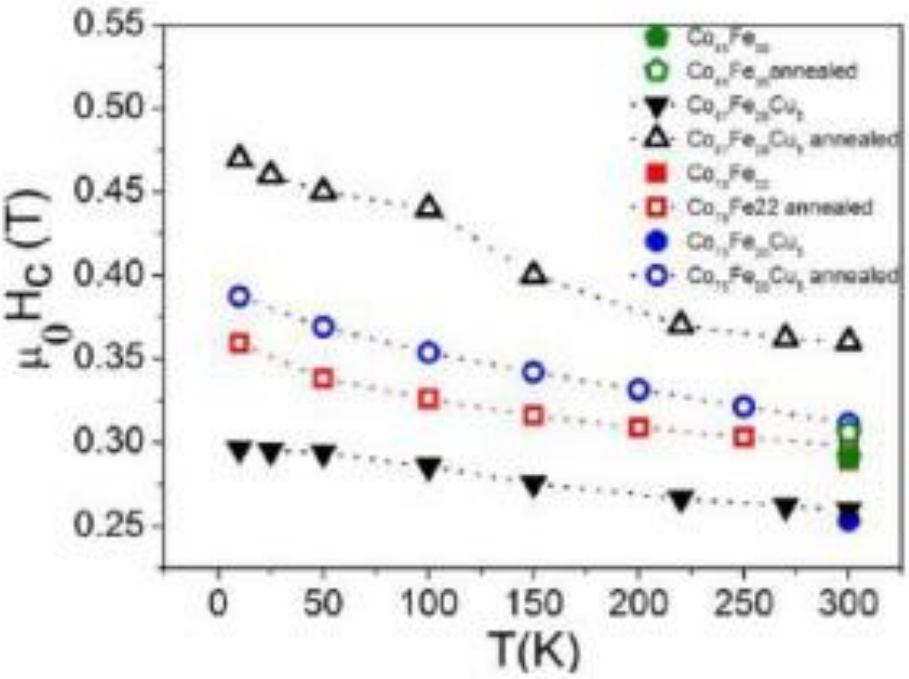

Fig 30: Temperature dependence of coercivity for several CoFe and CoFeCu nanowires (DNW=18 nm) in their as-prepared state and after optimal annealing.

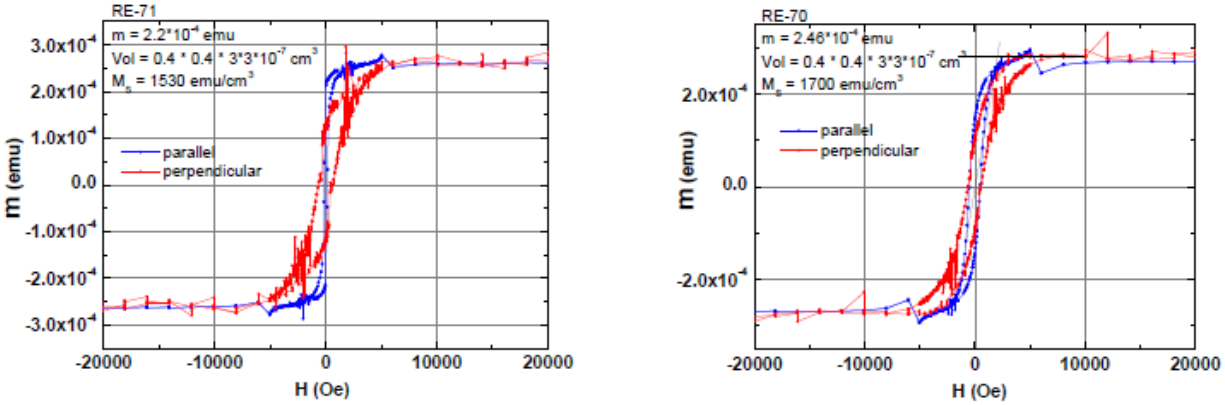

Fig 31. SQUID measurements of $[AuCu/Fe_{45}Co_{55}(C)]_{n=3}$ *samples.*

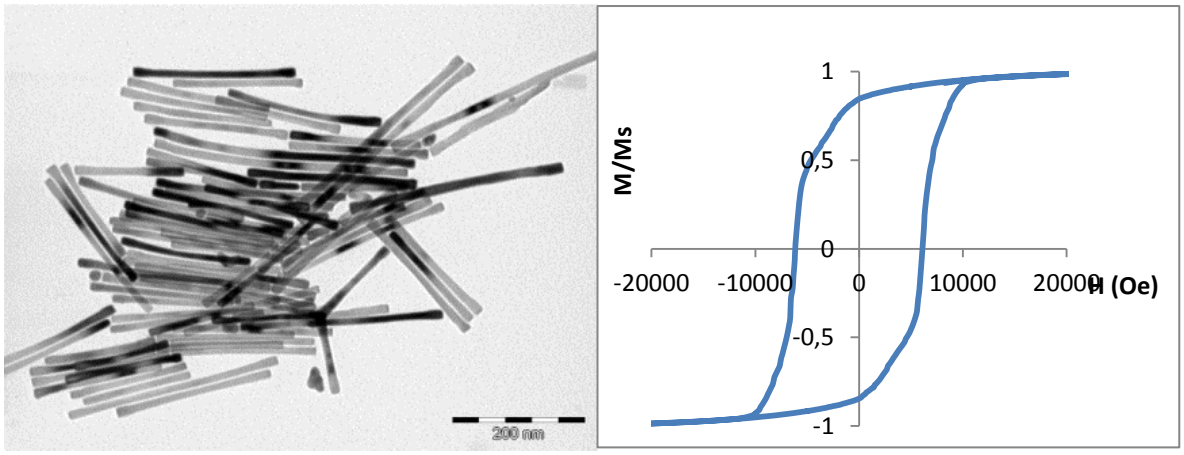

Figure 32: (a) TEM image of cobalt nanorods prepared at a scale of 10 g in 2L of butanediol using a 3L jacketed reactor; (b) magnetization curve of an assembly of the rods measured with the applied field parallel to the rod long axis.

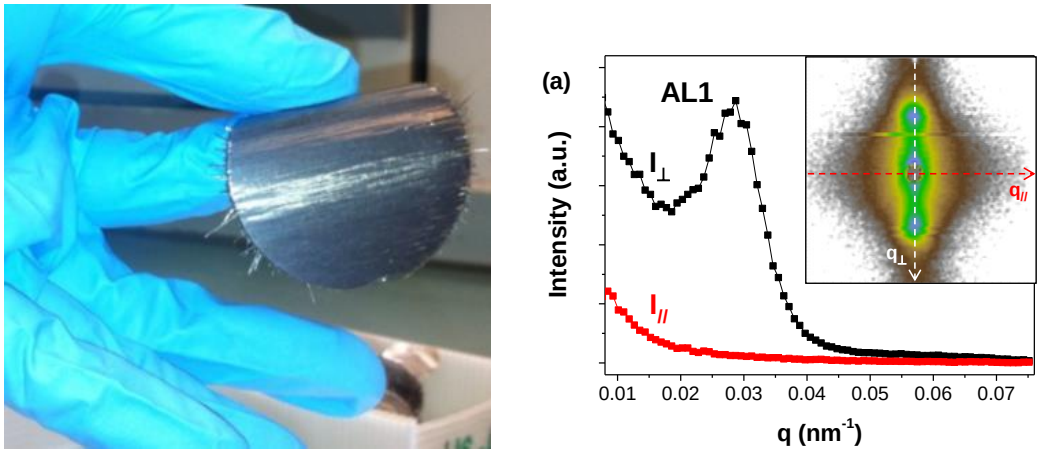

Figure 33: (a) wafer of cobalt nanorods obtained by drying a suspension in chloroform under an external magnetic field of 1T; (b) Small angle neutron intensity profile scattered by a cobalt nanorod assembly, perpendicular (black square) and parallel (red diamond) to the rod alignment. Inset: corresponding 2D SANS pattern. The two correlation spots scattered perpendicularly to the rods show a very good rod ordering in the assembly.

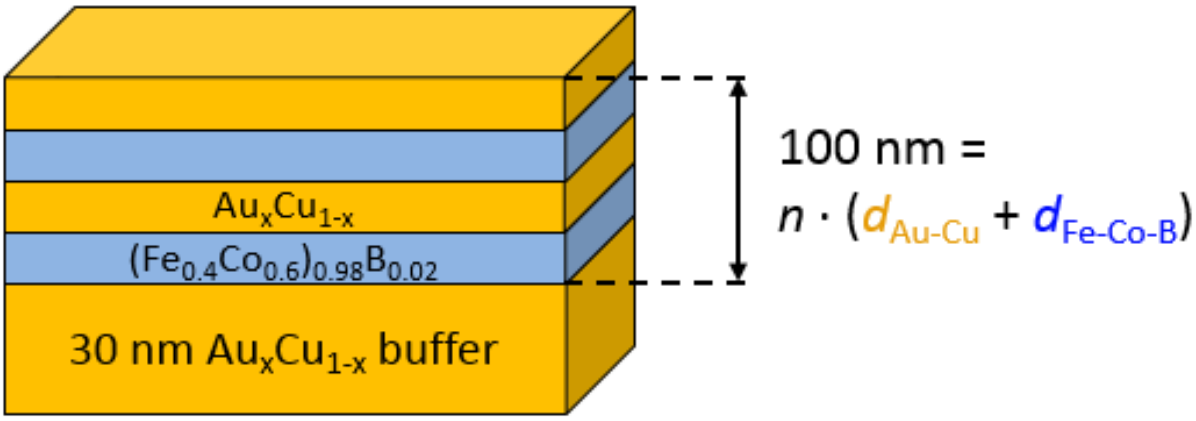

Figure 34: Schematic architecture of the multilayers. The overall multilayer thickness is 100 nm for reasons of comparability.

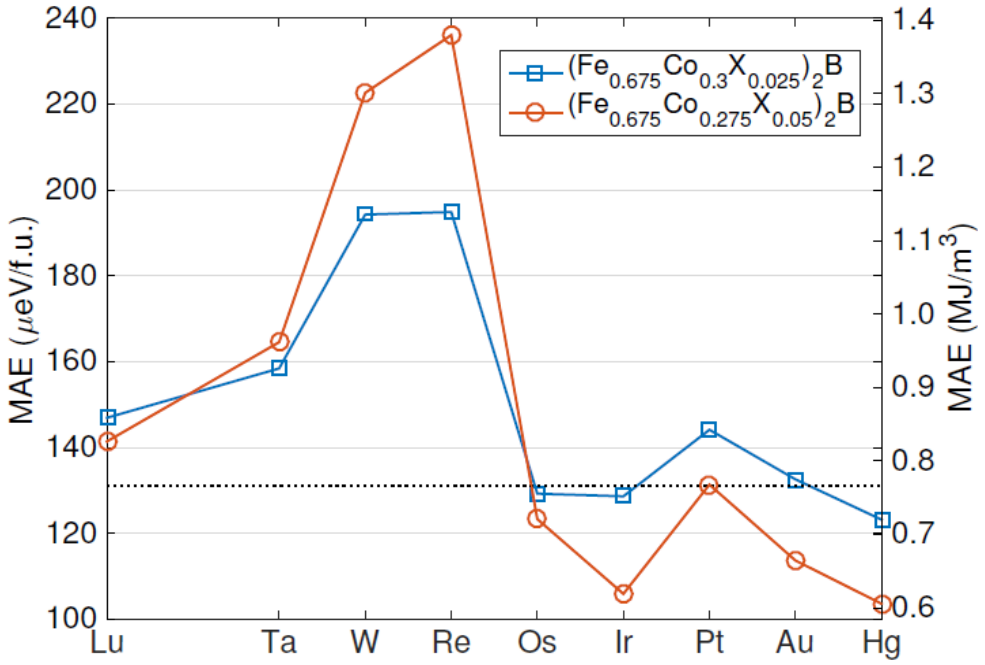

Figure 35: MAE for various elements X in $(Fe_{0.675}Co_{0.3}X_{0.025})_2B$ and $(Fe_{0.675}Co_{0.275}X_{0.05})_2B$. The dotted line indicates the MAE of $(Fe_{0.7}Co_{0.3})_2B$ for comparison.

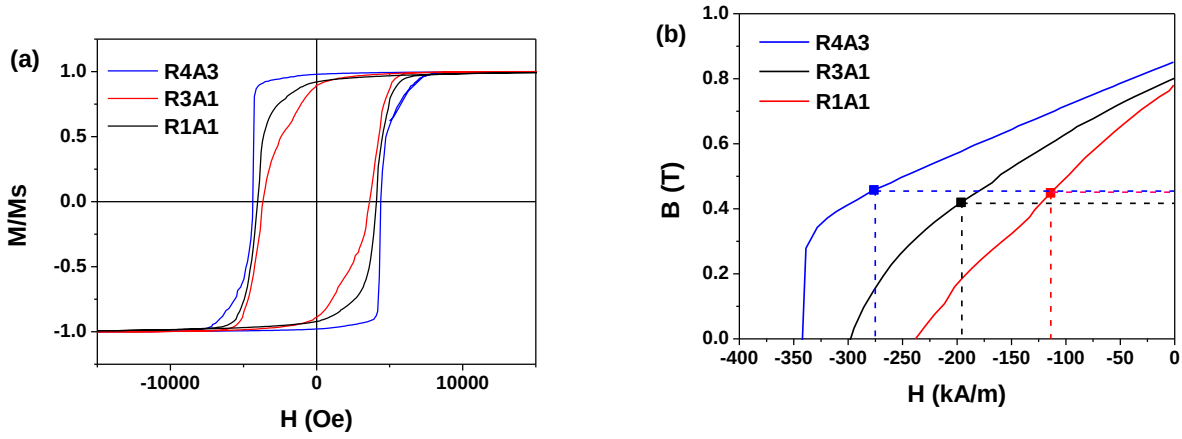

Figure 36: Hysteresis loop (a) and second quadrant of the corresponding B(H) loop (b) of three rod alignments exhibiting the same magnetic volume fraction: (blue) d_m = 22 nm, volume fraction = 48.7%, BH_{max} = 126 kJ.m^{-3} ; (black) d_m = 24 nm, volume fraction = 48.7%, BH_{max} = 82.5 kJ.m^{-3}; (red) d_m = 28 nm, volume fraction = 48.8%, BH_{max} = 51 kJ.m^{-3}.

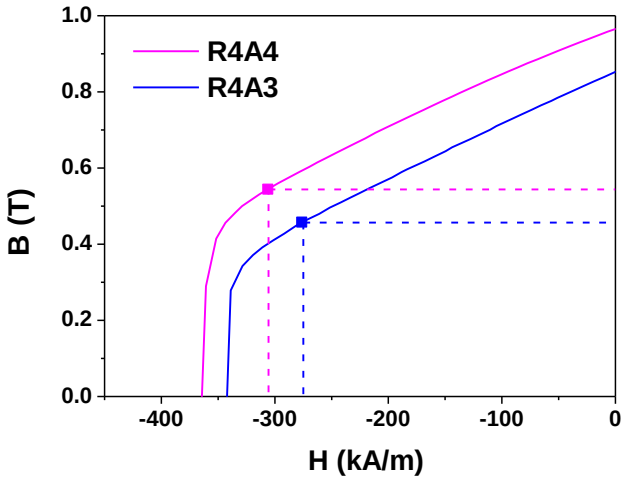

Figure 37: Second quadrant of the B(H) loop of two assemblies of the same cobalt nanorods (d_m = 22 nm) with a magnetic volume fraction V_M = 48.7% and a BH_{max} = 126 kJ.m^{-3} (blue) and a magnetic volume fraction V_M = 54.4% and a BH_{max} = 167 kJ.m^{-3} (magenta).

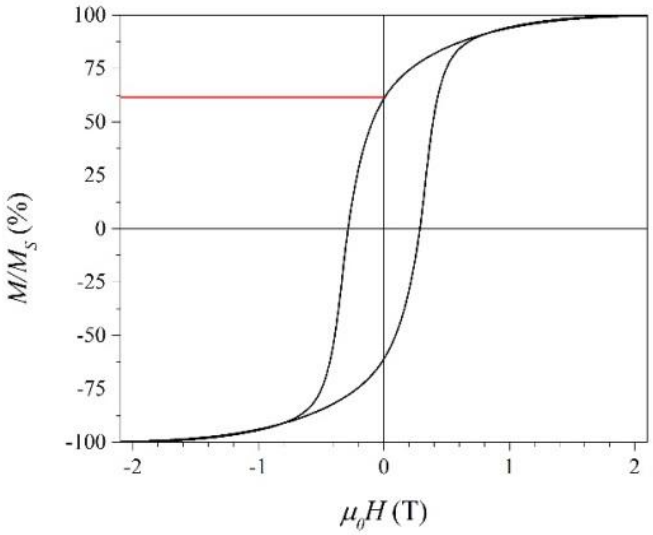

Figure 38: Room temperature pulse magnetometer measurements of hot compacted Co nanowires.

(a)

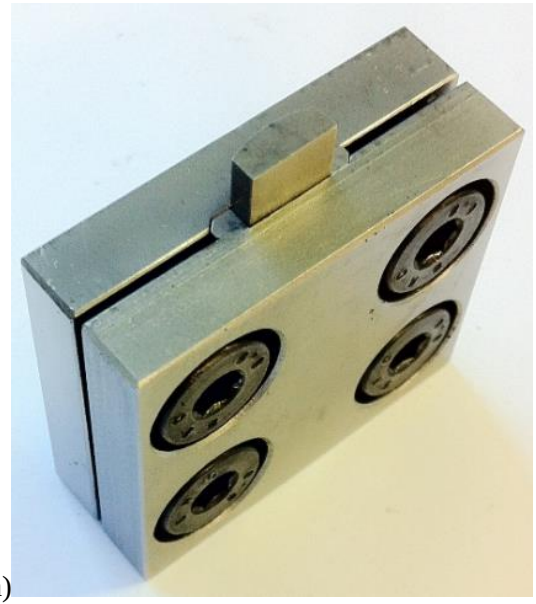

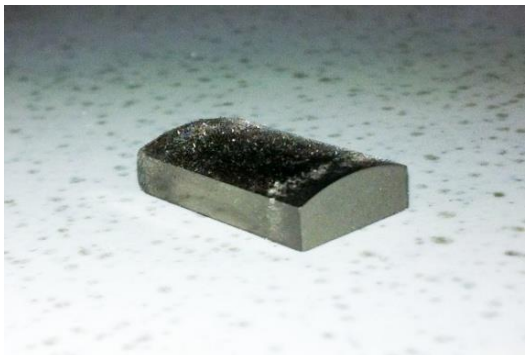

(b)

Fig. 39 Images of the press die (a) and the final magnet (b)

Figure 40: Examples of pre-aligned needles/platelets obtained in the 5mm width parallelepiped mold.

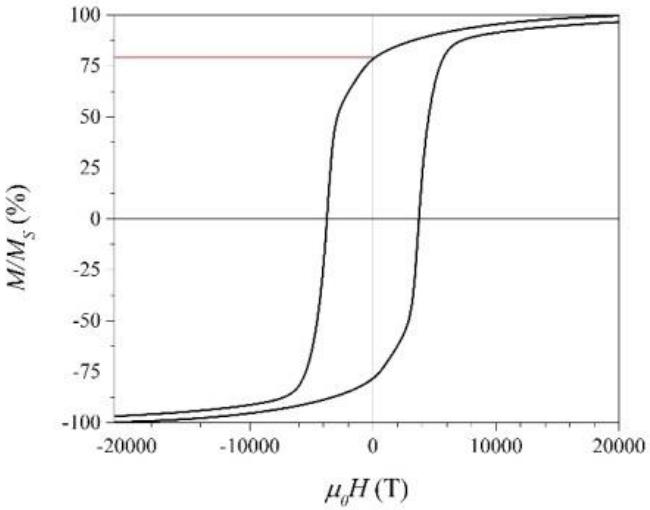

Figure 41: *Room temperature pulse magnetometer measurements of Co nanowire needles after SPS.*

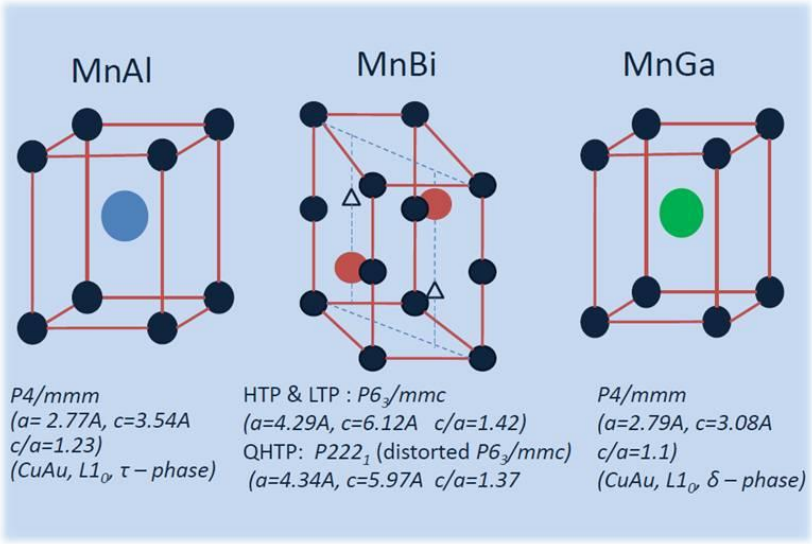

Fig. 42 Various candidate structures of Mn-Based alloys

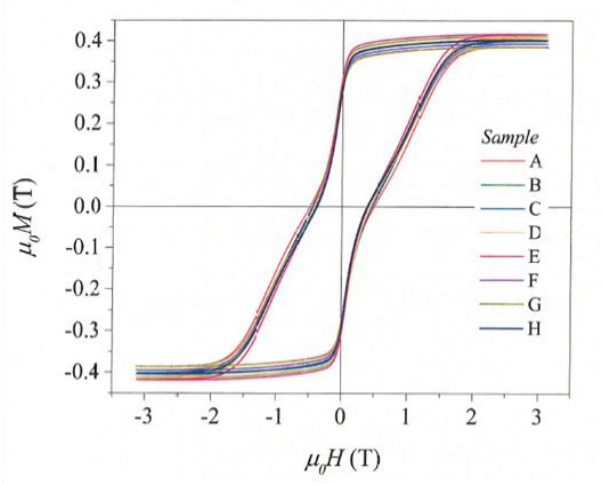

Fig. 43 The Optimized magnets showing uniformity and their characteristic properties.

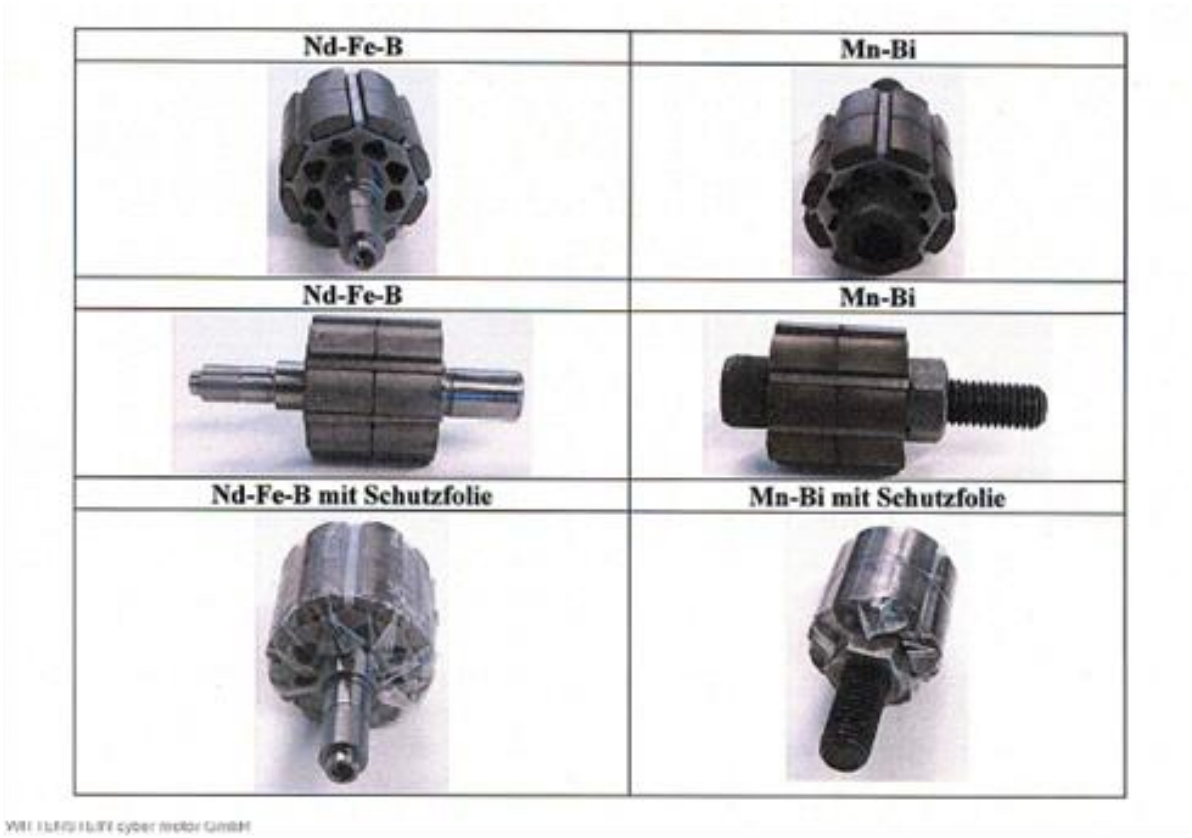

Fig. 44 MnBi and NdFe B magnets glued on the test-motor

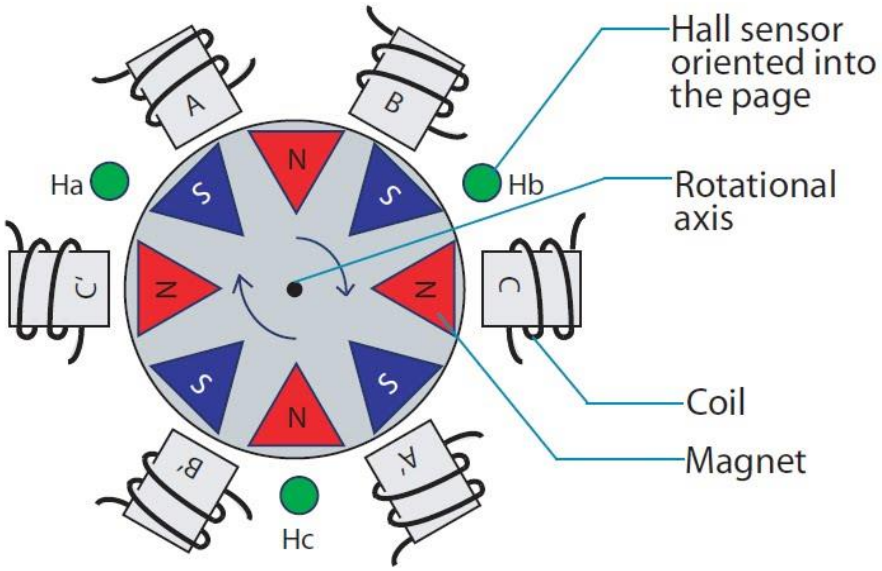

Fig. 45 Schematic of a 8-pole motor with PM mounted on the rotor different magnetization orientation. We run the motor at ~ 700 and 1000 rpm and the results are given below

Mn-Bi (n=737 min-1 Uieff=0,7378V; Uieff (1000min-1) = 1,001V

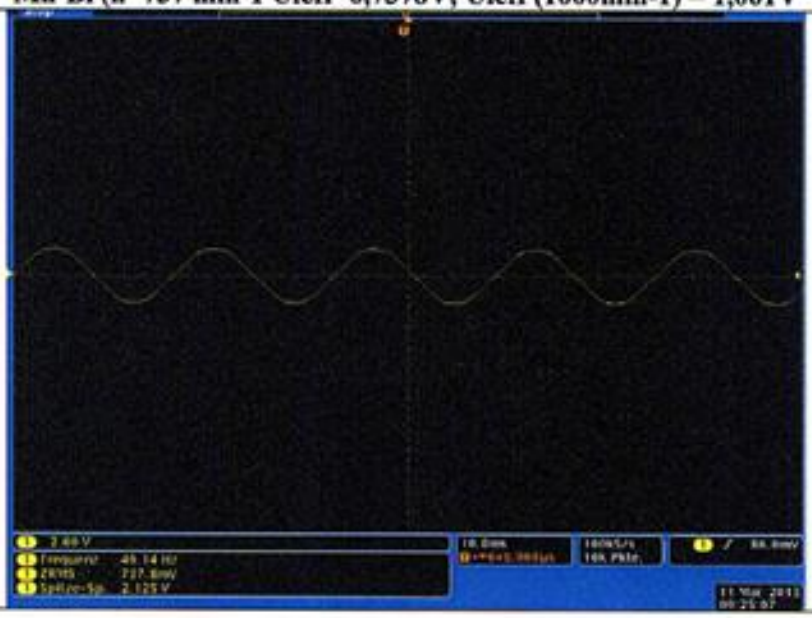

Nd-Fe-B mit Schutzfolie (n=667 min-1 Uieff=2,717V) ; Uieff (1000min-1) = 4,073V

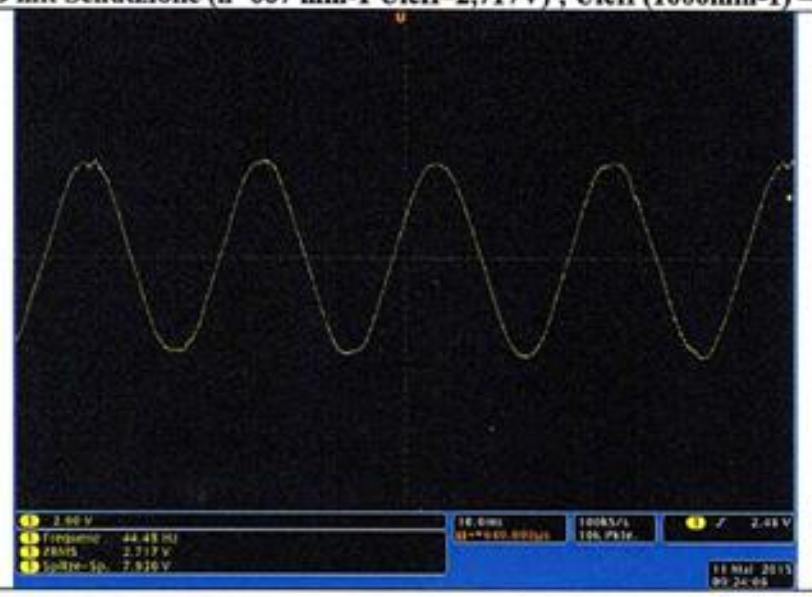

Performance of the motor with MnBi and NdFeB magnets

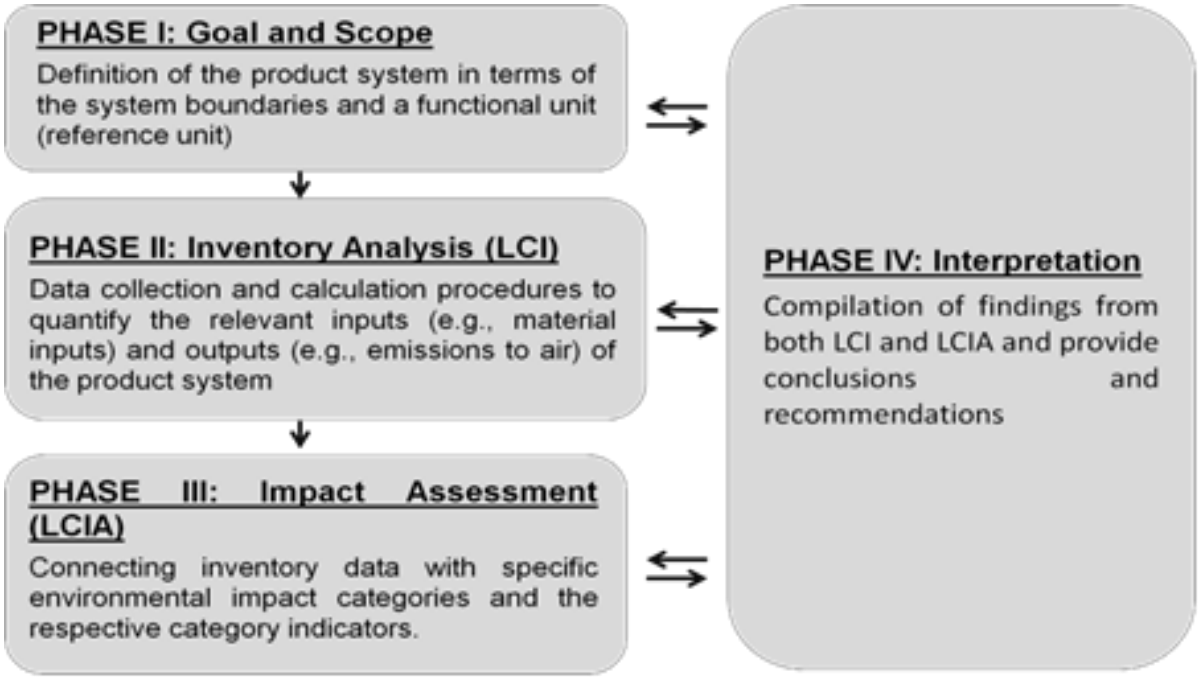

Figure 46 . *Methodology and steps for LCA studies according to ISO:14044:2006*
should be prioritized and secondary data from databases and literature will be used when needed.

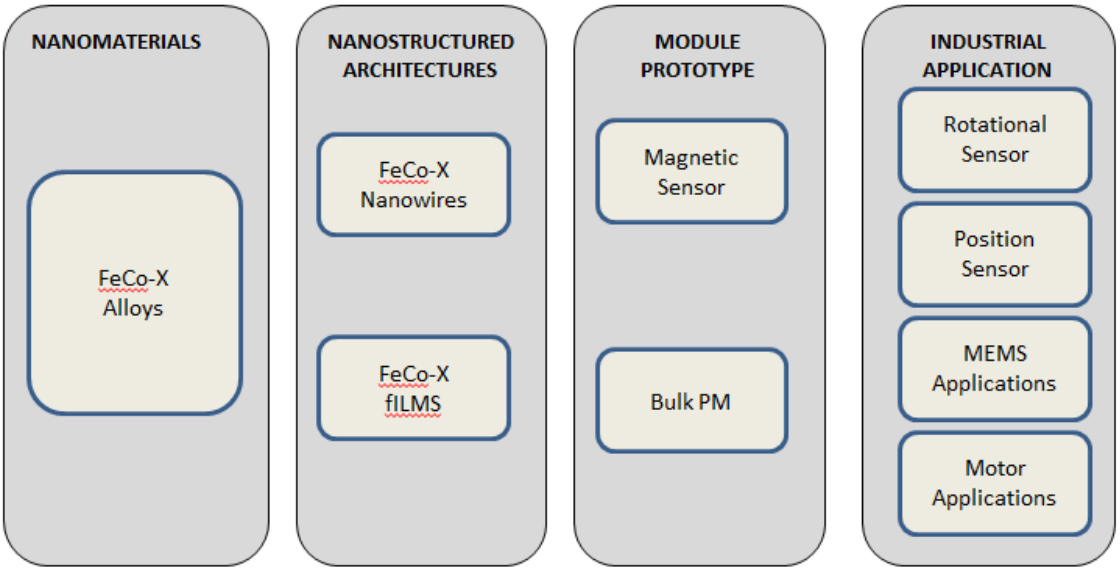

Figure 47 . *Preliminary scope of FeCo-X systems*

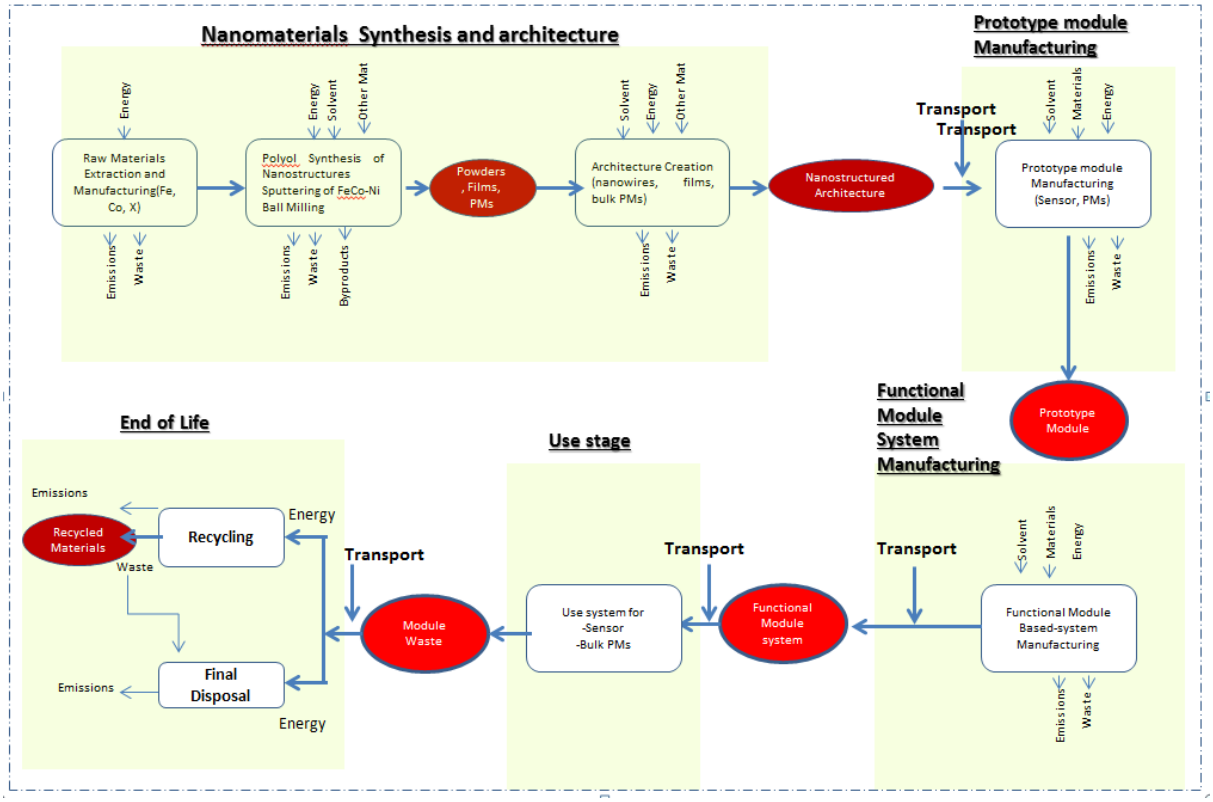

Fig. 48. System flowchart for Applications

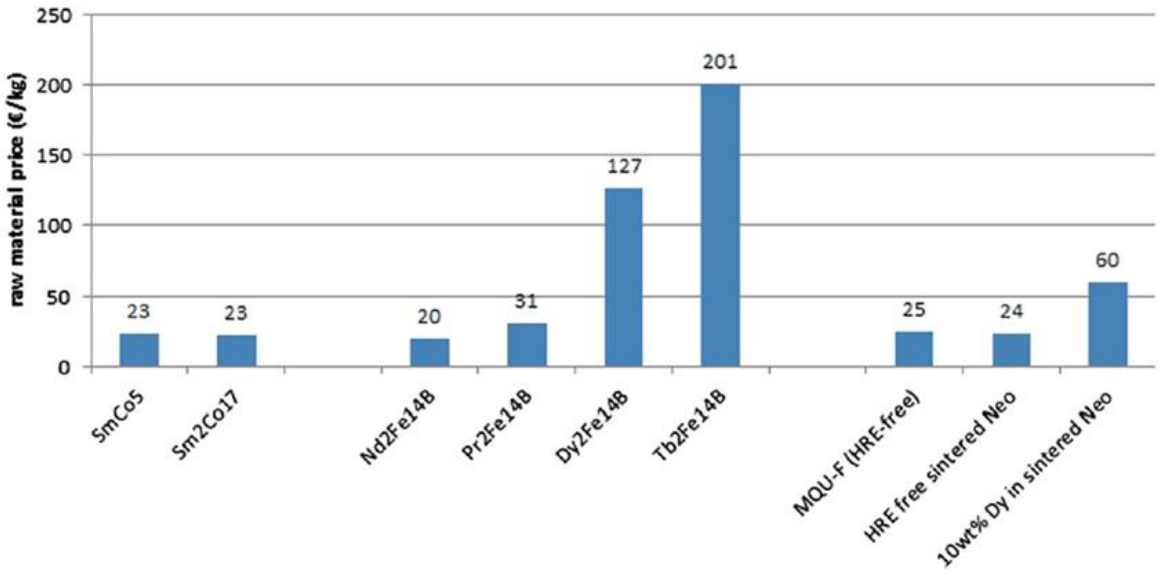

Fig.49. Raw material prices of several RE-based PMs alloys (after P. McGuinness, 2015)

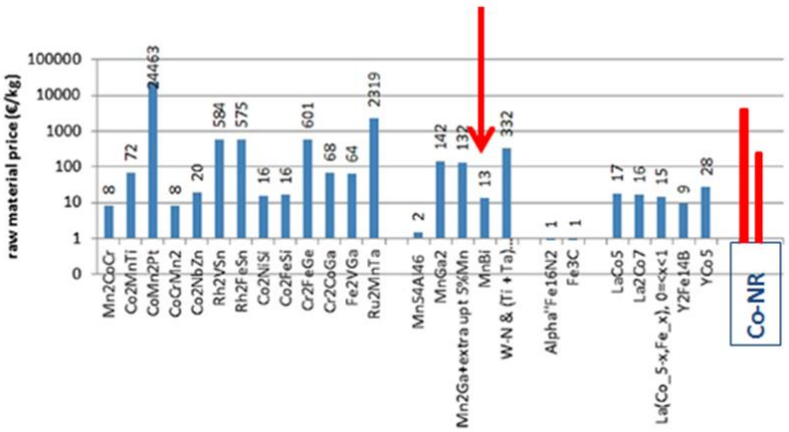

Fig. 50 RE-Free alloys estimated cost for prices No 2013-April 2014 (after P. McGuinness, 2015).

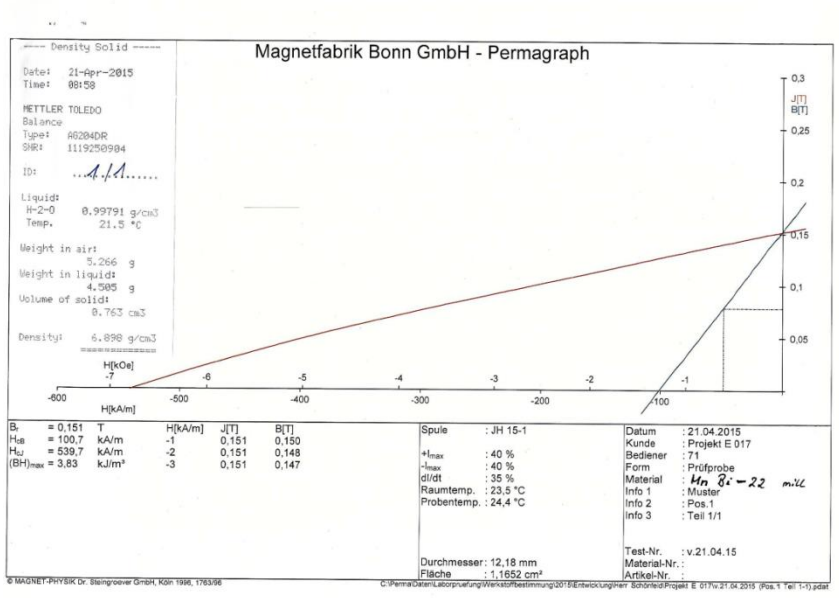

Fig. 51 Typical BH-loops of MnBi-bonded magnets